

Simulations of the 21 cm emission line for upcoming large-scale H I galaxy surveys

Joël Mayor^{1*}, Marta Spinelli^{2,3}, Gabriella De Lucia^{4,5}, Robert Yates⁶, Alexandre Refregier¹,
Fabio Fontanot^{4,5}, Lizhi Xie⁷, and Michaela Hirschmann^{8,4},

¹*Institute for Particle Physics and Astrophysics, ETH Zürich, Wolfgang-Pauli-Strasse 27, 8093 Zürich, Switzerland*

²*Observatoire de la Côte d'Azur, Laboratoire J-L Lagrange, Boulevard de l'Observatoire, Nice, France*

³*Department of Physics and Astronomy, University of the Western Cape, Cape Town 7535, South Africa*

⁴*INAF - Astronomical Observatory of Trieste, via G.B. Tiepolo 11, I-34143 Trieste, Italy*

⁵*IFPU - Institute for Fundamental Physics of the Universe, via Beirut 2, 34151, Trieste, Italy*

⁶*Centre for Astrophysics Research, University of Hertfordshire, Hatfield, AL10 9AB, UK*

⁷*Astrophysics Center, Tianjin Normal University, Binshuixidao 393, 300387, Tianjin, China*

⁸*EPFL - Institute of Physics, Laboratory for Galaxy Evolution, Observatoire de Sauverny, Chemin Pegasi 51, 1290 Versoix, Switzerland*

Accepted XXX. Received YYY; in original form ZZZ

ABSTRACT

Upcoming galaxy surveys with the SKA Observatory will detect neutral hydrogen (H I) across unprecedented volumes, and their scientific return will crucially depend on predictive models for H I observables. In this work, we present a framework to simulate the neutral hydrogen 21 cm emission line in such large-scale H I galaxy surveys. This framework is developed as a modular layer that builds on semi-analytical models. In particular we use as bases the Galaxy Evolution and Assembly (GAEA) and L-Galaxies semi-analytical models, coupled to merger trees from the Millennium Simulation suite. We validate our framework against local Universe observations, demonstrating consistency with velocity functions, and generalised Tully-Fisher relations. Predictions based on GAEA and L-Galaxies exhibit mutual consistency despite the distinct underlying physical prescriptions. We construct mock galaxy catalogues that incorporate forward-modelled selection functions, inclination effects, and redshift broadening, reproducing the statistical distributions of H I-selected galaxies in the ALFALFA survey. Finally, we present redshift distribution forecasts for future SKA Observatory H I galaxy surveys. This framework offers a flexible tool for interpreting upcoming large-scale radio surveys and studying H I line observables as cosmological probes.

Key words: radio lines: galaxies – line: profiles – software: simulations

1 INTRODUCTION

Observations of atomic neutral hydrogen (H I) through its characteristic 21 cm hyperfine transition emission line are key for extragalactic astrophysics (e.g. Kerr et al. 1954; Giovanelli & Haynes 1988), providing unique insights that complement optical and infrared observations especially in tracing diffuse, dust-obscured gas (e.g. Wilson et al. 2013).

Within galaxies, H I is the dominant atomic phase of the cold interstellar medium and fuels the baryon cycle between the circumgalactic medium and the star-forming disc via accretion, cooling, and feedback-driven recycling (e.g. Kereš et al. 2005; Dekel & Birnboim 2006; Fraternali & Binney 2008; Sancisi et al. 2008; Tumlinson et al. 2017). In sufficiently dense, shielded and metal-enriched regions, H I converts to molecular hydrogen (H₂), providing the immediate fuel for star formation (e.g. Hollenbach & Salpeter 1971; Blitz & Rosolowsky 2006; Krumholz et al. 2009; Gnedin & Kravtsov 2011; Cortese et al. 2017). Mapping the H I content and distribution in individual galaxies therefore provides a crucial tool for understanding galactic assembly and evolution, the regulation of star formation, and

phase transitions within the interstellar medium (e.g. Gunn & Gott 1972; Boselli & Gavazzi 2006; Bigiel et al. 2008; Kennicutt & Evans 2012).

Moreover, the 21 cm emission line enables kinematic studies. For spatially resolved interferometric observations, synthesis imaging delivers rotation curves and gas-velocity dispersion fields that constrain dynamical mass profiles and the impact of pressure support (e.g. Begeman 1989; Sofue & Rubin 2001; de Blok et al. 2008; Lelli et al. 2016). For unresolved detections, integrated H I profiles capture global dynamics (e.g. Tully & Fouque 1985) and yield rotational velocity estimates through measurements of their width.

In particular, the Tully-Fisher (TF) relation is a correlation between H I profile widths and optical magnitudes of spiral galaxies which was originally defined by Tully & Fisher (1977). Its generalizations include any empirical correlation between proxies of the rotational motion and proxies of the intrinsic luminosity of a galaxy. An example is the baryonic Tully-Fisher (bTF) relation (e.g. McGaugh et al. 2000; Bell & de Jong 2001; McGaugh 2005; Lelli et al. 2019). In galaxy evolution studies, the TF/bTF relations are used to constrain the coupling between halos, discs, and feedback, the role of angular momentum, and the balance of rotation and pressure support. In the framework of cosmological studies, the TF/bTF relations

* E-mail: jmayor@ethz.ch

provide luminosity distance estimates (e.g. [Sorce et al. 2014](#)), enabling the construction of peculiar-velocity catalogues (e.g. [Springob et al. 2007](#); [Tully et al. 2023](#)). These catalogues can be employed to probe the cosmic growth rate via velocity–density comparisons, test gravity at cosmological scales, and contribute to H_0 determinations (e.g. [Kourkchi et al. 2022](#); [Watkins et al. 2023](#); [Boubel et al. 2025, 2024a,b](#)). The precision of such distance estimates depends critically on the accuracy with which H I line profiles can be modelled, making a robust predictive framework a prerequisite for cosmology studies with peculiar velocities.

H I-selected galaxy surveys can thus provide independent and synergistic constraints on cosmological models alongside optical/near-infrared spectroscopic programs such as SDSS/BOSS/eBOSS ([York et al. 2000](#); [Dawson et al. 2013, 2016](#); [Almeida et al. 2023](#)), DESI ([DESI Collaboration et al. 2016, 2025](#)), 4HS ([Taylor et al. 2023](#)), and Euclid ([Laureijs et al. 2011](#); [Euclid Collaboration et al. 2025](#)) through ‘classical’ galaxy clustering probes like baryon acoustic oscillations and redshift-space distortions, and via peculiar velocity measurements (e.g. [Koda et al. 2014](#); [Howlett et al. 2017](#); [Howlett 2019](#); [Qin et al. 2019, 2025](#)).

The observational landscape for H I galaxy studies, built on surveys such as the H I Parkes All-Sky Survey (HIPASS, [Barnes et al. 2001](#); [Meyer et al. 2004](#)), and the Arecibo Legacy Fast ALFA Survey (ALFALFA, [Giovannelli et al. 2005](#); [Haynes et al. 2011, 2018](#)), is undergoing rapid transformation with the advent of SKA Observatory (SKAO) pathfinder instruments, such as the Australian SKA Pathfinder (ASKAP) and the Meer-Karoo Array Telescope (MeerKAT). Ongoing and planned programs, including WALLABY and DINGO (ASKAP, [Johnston et al. 2008](#); [Duffy et al. 2012a,b](#); [Koribalski et al. 2020](#)), LADUMA and MIGHTEE-HI (MeerKAT, [Blyth et al. 2016](#); [Jarvis et al. 2016](#); [Maddox et al. 2021](#)), CHILES (VLA, [Fernández et al. 2013, 2016](#)), and CRAFTS/FASHI (FAST, [Zhang et al. 2019, 2024](#)), are delivering unprecedented combinations of sensitivity, area, and depth. Looking ahead, future infrastructures, specifically the SKAO, promise routine detections to higher redshifts and statistical samples suitable for studies of galaxy evolution and the cosmic large-scale structure (e.g. [Yahya et al. 2015](#); [Braun et al. 2019](#); [Weltman et al. 2020](#); [Murphy et al. 2018](#)).

As ongoing and next-generation H I galaxy surveys enter this new era of statistical samples, fully exploiting the growing datasets requires theoretical frameworks that include the physical processes underlying the emergence of scaling relations such as the TF/bTF, and that are capable of predicting their full shape, i.e. the median relations, their scatter, outliers, and evolution with redshift and environment. In particular, such frameworks are essential for understanding and constraining systematics in the TF/bTF relations as a distance indicators and ultimately in peculiar velocity cosmology. This motivates modern, predictive models for H I observables, capable of both reproducing currently available data and forecasting future surveys.

Simulation based modelling of H I distribution in galaxies presents unique challenges. Hydrodynamical simulations, e.g. EAGLE ([Schaye et al. 2015](#)), IllustrisTNG ([Springel et al. 2018](#)), BAHAMAS ([McCarthy et al. 2017](#)), SIMBA ([Davé et al. 2019](#)), NEWHORIZON ([Dubois et al. 2021](#)), FLAMINGO ([Schaye et al. 2023](#)), CROCODILE ([Oku & Nagamine 2024](#)), incorporate detailed baryonic physics but remain computationally expensive for exploring large parameter spaces over cosmological volumes. In addition, the dynamical range needed for a full self-consistent treatment of H I exceeds the limits of present-day state-of-the-art hydrodynamical simulations. Despite significant advancements in the interstellar medium (ISM) treatment, H I is thus typically a post-processing out-

put in cosmological scale simulations (e.g. [Diemer et al. 2018](#)), except for very small volumes, i.e. in [Chaikin et al. \(2025\)](#).

Semi-analytical models (SAMs) offer a complementary approach, enabling efficient simulations of the large-scale assembly and evolution of galaxies across cosmic time. At their core, contemporary SAMs, such as GAEA ([De Lucia et al. 2024](#); [Fontanot et al. 2025](#)), L-Galaxies ([Yates et al. 2024](#)), GALFORM ([Lacey et al. 2016](#)), SHARK ([Lagos et al. 2018](#)), SAG ([Cora et al. 2018](#)), GABE ([Jiang et al. 2019](#)), the Santa Cruz SAM ([Yung et al. 2023, 2022](#)), and DarkSAGE ([Stevens et al. 2024](#)), are built upon merger trees derived from large and high-resolution dark-matter-only N-body simulations. Within this dark matter structure, baryonic physics is incorporated in a post-processing stage using a set of prescriptions, based on phenomenologically and/or theoretically motivated arguments, for a wide array of astrophysical processes. SAMs are designed to rapidly explore the parameters space associated with these baryonic processes, tracing the evolution of key galaxy properties and observables for large statistical samples on scales both relevant for cosmology in terms of volume and for galaxy evolution studies in terms of resolution.

In their seminal work, [Obreschkow et al. \(2009a\)](#) used empirical relations to partition, in post-processing, cold hydrogen as predicted by a then state-of-the-art SAM ([De Lucia & Blaizot 2007](#), a precursor of GAEA). The approach allowed the construction of large mock catalogues including H I masses and an explicit modelling the 21 cm line profiles. Later independent efforts led to an explicit and self-consistent inclusion of the partition of the cold gas in its molecular and atomic components in several SAMs (e.g. [Fu et al. 2010](#); [Lagos et al. 2011](#); [Somerville et al. 2015](#); [Xie et al. 2017](#)), which also yielded advancements in prescriptions for star formation and associated processes. In particular, some of these models now implement star formation prescriptions based on the H₂ surface density, that is a better tracer of star forming regions ([Bigiel et al. 2008](#)). In the meantime, new observational data from H I surveys, such as ALFALFA ([Haynes et al. 2018](#)), have provided updated constraints on H I scaling relations and statistics that are essential to calibrate state-of-the-art SAMs.

A few studies have developed frameworks inspired by [Obreschkow et al. \(2009a,b\)](#) to simulate H I-selected galaxy observations. For example, [Trujillo-Gomez et al. \(2011\)](#) and [Desmond \(2012\)](#) assigned modelled 21cm lines to galaxy catalogues built using a Halo Abundance Matching (HAM) technique. More recently, predictions based on the SHARK SAM, in combination with the SURFS simulations suite ([Elahi et al. 2018](#)) and a modelling of the H I line profiles, have been used to carry out comparisons with ALFALFA data ([Chauhan et al. 2019](#)), and to make forecast studies for the WALLABY survey ([Koribalski et al. 2020](#)).

In this work, we build a framework to associate H I emission lines with galaxies from two state-of-the-art semi-analytical models, GAEA ([De Lucia et al. 2024](#)) and L-Galaxies ([Yates et al. 2024](#)), both evaluated in post processing of the Millennium Simulation suite ([Springel et al. 2005](#); [Boylan-Kolchin et al. 2009](#)). The use of two independent SAMs with distinct baryonic prescriptions provides a built-in robustness check. The result is a simulation pipeline for H I-selected galaxy surveys, which we test and validate through thorough comparisons with existing observational data, in particular for generalised Tully-Fisher relations, and which we use as a predictive tool to present forecasts for SKAO H I galaxy surveys.

The paper is structured as follows: In section 2, we summarize the semi-analytical models and implementations relevant for this study. In section 3, we describe our model for the H I 21 cm emission line. In section 4 we build mock H I galaxy catalogues and compare our

simulations predictions with empirical data, first at the SAM output level, and then also by forward-modelling observational effects. We discuss the results in section 5. Finally, we leverage our predictive framework to forecast the redshift distribution for SKAO H I galaxy redshift surveys in section 6.

2 SIMULATIONS

2.1 Dark Matter N-body Simulations

In this work, SAMs are coupled with the reconstructed merger history of dark matter halos, i.e. merger trees, extracted from two different underlying dark matter N -body simulations, namely those of the Millennium Simulation I (MSI, Springel et al. 2005), and of the Millennium Simulation II (MSII, Boylan-Kolchin et al. 2009). These merger trees are structured as sample of ‘snapshots’ from the simulation volume at discrete redshifts, where each snapshot is a catalogue of dark-matter haloes. The cosmological model adopted in the MSI and MSII is based on a combined analysis of the 2dFGRS (Colless et al. 2001) and first-year WMAP data (Spergel et al. 2003) with parameters $\Omega_b = 0.0455$, $\Omega_m = 0.25$, $\Omega_\Lambda = 0.75$, $h = 0.73$, $\sigma_8 = 0.9$, and $n = 1$ (but see Section 2.2.2). The MSI traces $2160^3 \approx 10^{10}$ DM particles of mass $8.61 \cdot 10^8 M_\odot/h$ over redshifts $z \in [0, 127]$ in a cubic volume of $(500 \text{ Mpc}/h)^3$ with periodic boundary conditions. For the MSII, the number of DM particles is identical but the box size is $(100 \text{ Mpc}/h)^3$, which brings the mass resolution to $6.88 \cdot 10^6 M_\odot/h$.

2.2 Semi-Analytic Models

In this study, we develop predictions based on two distinct semi-analytic models, GAEA and L-Galaxies. The mutual consistency between predictions using either SAM serves as a robustness test. As will be developed, the fiducial cosmological models used in both SAMs are also distinct. However this has limited impact on the observables this study focuses on since the parameters of both SAMs are tuned based on similar empirical data, i.e. the differences in cosmology are absorbed in the tuning of the baryonic processes. SAM standard outputs are built on top of merger trees in the form of ‘snapshot’ galaxy catalogues, i.e. galaxy properties are saved at the same discrete redshift intervals.

2.2.1 GAEA

For the GALaxy Evolution and Assembly (GAEA) semi-analytical model (De Lucia et al. 2014; Hirschmann et al. 2016; Xie et al. 2017; Fontanot et al. 2020; Xie et al. 2020; De Lucia et al. 2024; Fontanot et al. 2025), we use the version presented in De Lucia et al. (2024) as reference. It reproduces several important observational constraints: (i) the evolution of the galaxy stellar mass function up to $z \sim 7$ and of the cosmic star formation rate density up to $z \sim 10$ (Fontanot et al. 2017); (ii) the measured correlation between stellar mass/luminosity and metal content of galaxies in the local Universe, down to the scale of Milky Way satellites (De Lucia et al. 2014; Hirschmann et al. 2016); (iii) the evolution of the galaxy mass–gas metallicity relation up to redshift $z \sim 3.5$ (Fontanot et al. 2021); (iv) the measured H I mass function and clustering of H I-rich galaxies (Zoldan et al. 2017; Spinelli et al. 2020; Fontanot et al. 2025); (v) the size–mass relation and the specific angular momentum–mass relation of late type and early type galaxies in the local Universe (Zoldan et al. 2018), as well as the evolution of the size–mass relation up to $z \sim 2$ (Zoldan et al. 2019). (vi) the H I mass – stellar mass scaling relation for both central

and satellite galaxies at $z = 0$ (Xie et al. 2020). (vii) the declining trend of H I fractions of satellite galaxies in cluster halos (Chen et al. 2024). (viii) the emission line properties of both star forming and AGN galaxies (Euclid Collaboration et al. 2024). In this study, we use model outputs based on the MSI and MSII that, as discussed above, assume a cosmological model consistent with WMAP1.¹

2.2.2 L-Galaxies

Like GAEA, L-Galaxies (Guo et al. 2011; Henriques et al. 2015, 2020; Yates et al. 2024) is built to run on the merger trees generated from the MSI and MSII N-body simulations. However, the corresponding merger trees have been re-scaled to match a *Planck* 2013 cosmology: $\Omega_{\Lambda,0} = 0.685$, $\Omega_{m,0} = 0.315$, $\Omega_{b,0} = 0.0487$, $\sigma_8 = 0.826$, $n_s = 0.96$, $h = 0.673$, using the technique described in Angulo & White (2010) and Angulo & Hilbert (2015).

The L-Galaxies version adopted in this work (Yates et al. 2024) includes the following advanced prescriptions: (i) an H I – H2 partitioning model following the McKee & Krumholz (2010) metallicity- and density-dependent formalism (Fu et al. 2010); (ii) radially resolved gas and stellar discs which are self-consistently evolved across all timesteps (Fu et al. 2013); (iii) a galaxy chemical enrichment (GCE) model accounting for binary stellar evolution and 118 individual chemical elements (Yates et al. 2013, 2024); and (iv) an explicit dust production and destruction model (Vijayan et al. 2019; Yates et al. 2024).

L-Galaxies free parameters are constrained on the observed stellar mass function and quenched fraction at $z = 0$ and 2, as well as the H I mass function at $z = 0$, using a Monte Carlo Markov Chain (MCMC) formalism (Henriques et al. 2020). The model reproduces several other important observations, including (i) the H I mass – stellar mass scaling relation at $z = 0$ (Henriques et al. 2020); (ii) the chemical composition of the stars, interstellar medium (ISM), and circumgalactic medium (CGM) in local galaxies, including radial profiles (Yates et al. 2021a); (iii) the cosmic metal and SFR density back to $z \sim 5$ (Yates et al. 2021b); and (iv) the evolution of the mass – metallicity relation and dust-to-gas ratios back to $z \sim 4$ (Yates et al. 2024).

3 EMISSION LINE MODEL

Accurate modelling of H I line profiles underpins Tully-Fisher distance estimates and their precision, and is therefore central to cosmological applications. In the following, we present the method we adopt, inspired from Obreschkow et al. (2009a) and Chauhan et al. (2019), to associate a 21 cm emission line to the galaxies in SAM output catalogues. We detail all specific assumptions in our implementation.

3.1 Model 21cm flux

The rest-frame flux density profile of an H I galaxy’s 21cm emission line is constructed as the product of a distribution, the normalised

¹ In the recent work by Fontanot et al. (2025) (see also Cantarella et al. 2025), the GAEA SAM has also been run on merger trees from the P-Millennium simulation (Baugh et al. 2019) that adopts cosmological parameters consistent with first year Planck results.

line profile $\Psi_{\text{H I}}(V)$, and a scale, the velocity-integrated 21 cm flux $S_{21\text{cm}}^V$.

$$s(V) = S_{21\text{cm}}^V \cdot \Psi_{\text{H I}}(V) \quad (1)$$

The velocity-integrated flux, which fundamentally carries an observational dependence, is modelled as

$$S_{21\text{cm}}^V = \frac{(1+z)L_{21\text{cm}}^V}{4\pi D_L^2(z)} \quad (2)$$

where $D_L(z)$ is the luminosity distance between the source and the observer, and $L_{21\text{cm}}^V$ is the velocity-integrated rest-frame luminosity of the 21cm emission line. The latter, neglecting self-absorption or rather assuming the H I distribution to be optically thin, can be derived from fundamental atomic physics considerations as being proportional to the number of neutral hydrogen atoms, hence to the H I mass (e.g. Meyer et al. 2004; Catinella et al. 2010). In the following we use:

$$L_{21\text{cm}}^V [\text{Jy km s}^{-1} \text{Mpc}^2] = 5.319 \cdot 10^{-5} (M_{\text{H I}}/M_{\odot}). \quad (3)$$

The normalised line profile $\Psi_{\text{H I}}(V)$ encodes, simultaneously, information about both internal dynamics and the H I content. Therefore, its modelling depends both on galaxy properties and structure, as we describe next.

3.2 Model H I galaxies

Dark matter N-body simulations and semi-analytic models provide a number of properties for the simulated host DM halos and the associated galaxies. We use a set of these properties in our 21cm line modelling.

Specifically, from N-body simulations we use:

- R_{vir} and M_{vir} , the dark matter halo virial radius and mass.

In the Millennium-based merger trees used by GAEA and L-Galaxies, these are defined as the radius R_{200} of the largest sphere centered on the gravitational potential minimum which contains an overdensity larger than 200 times the critical density, and the total mass M_{200} within this sphere.

From the semi-analytic models, we use:

- $M_{\star, \text{b}}$ and $r_{\star, \text{b}}$, the stellar bulge mass and its radial scale length
- $M_{\star, \text{d}}$ and $r_{\star, \text{d}}$, the stellar disc mass and its radial scale length
- M_{g} and r_{g} , the total cold gas disc mass and its radial scale length
- M_{H} and R_{mol} (or f_{mol}), the total cold hydrogen mass and the ratio of molecular to atomic cold hydrogen (or the fraction of cold hydrogen in the molecular form).

Detailed definitions of these galaxy properties, specific to each SAM, can be found in De Lucia et al. (2024) for GAEA, and Yates et al. (2024) for L-Galaxies. Coupling them with simple structural assumptions allows us to build models for the distribution of H I within galaxies and associated dynamics, namely surface density profiles (section 3.2.1) and circular density profiles (section 3.2.2).

3.2.1 Neutral hydrogen surface density profile

GAEA assumes axially symmetric thin discs with exponential surface density profiles, both for the cold gas and the stellar disc components.

$$\Sigma_{\text{d}}(r) = \frac{M_{\text{d}}}{2\pi r_{\text{d}}^2} \exp\left(-\frac{r}{r_{\text{d}}}\right) \quad (4)$$

where M_{d} is the total mass contained in the disc (i.e. M_{g} or $M_{\star, \text{d}}$), and r_{d} is the corresponding scale length (i.e. r_{g} or $r_{\star, \text{d}}$). In L-Galaxies, an exponential profile is also assumed for the infalling gas onto the disc, while the density profiles of the stellar and cold gas discs are not constrained by any function form. They are divided-up into concentric rings, and the profile evolves self-consistently due to radial gas flows, star formation, etc.

The cold hydrogen mass M_{H} , i.e. the dominant component of cold gas mass M_{g} , is also estimated using different prescriptions in the two SAMs considered. In GAEA, it is computed assuming, at all cosmic epochs, the relative cosmic abundance of each element as predicted by big bang nucleosynthesis. Thus, hydrogen is assumed to account for a fixed 74% of cold gas ($M_{\text{H}} \equiv 0.74 M_{\text{g}}$), with remaining fraction assumed to be in the form of helium (He), dust and ionized gas. Cold hydrogen is assumed to be homogeneously distributed within the gaseous disc, hence also yielding an exponential surface density profile $\Sigma_{\text{H}}(r)$ (eq. 4) with scale length $r_{\text{H}} = r_{\text{g}}$.

In L-Galaxies, pristine gas in the intergalactic medium is also assumed to be 74% hydrogen, but the chemical composition of cold gas inside haloes and galaxies is then explicitly modelled and traced via the chemical evolution model (Yates et al. 2013), thus directly yielding M_{H} and $\Sigma_{\text{H}}(r)$ (for discrete rings).

Finally, the cold hydrogen disc is partitioned in its atomic (H I) and molecular (H₂) components. Recently published SAMs include different prescriptions for the cold gas partitioning and the evolution of the galaxies radial profile (e.g. Fu et al. 2010, 2013; Lagos et al. 2011; Somerville et al. 2015; Xie et al. 2017). The partition is typically expressed in terms of the ratio of molecular to atomic hydrogen surface densities $R_{\text{mol}}(r) = \Sigma_{\text{H}_2}(r)/\Sigma_{\text{H I}}(r)$, or equivalently in terms of the fraction of the hydrogen surface density in molecular form.

$$f_{\text{mol}}(r) = \frac{R_{\text{mol}}(r)}{(1 + R_{\text{mol}}(r))} = \frac{\Sigma_{\text{H}_2}(r)}{\Sigma_{\text{H}}(r)} \quad (5)$$

Thus yielding

$$\Sigma_{\text{H}_2}(r) = f_{\text{mol}}(r) \cdot \Sigma_{\text{H}}(r) \quad (6)$$

$$\Sigma_{\text{H I}}(r) = [1 - f_{\text{mol}}(r)] \cdot \Sigma_{\text{H}}(r) \quad (7)$$

Multiple hydrogen partitioning prescriptions have been explored (e.g. Blitz & Rosolowsky 2006; Krumholz et al. 2009; Krumholz 2013; McKee & Krumholz 2010) and shown to produce equivalent predictions for the global properties and distributions of model galaxies, both within the GAEA and L-Galaxies frameworks (Xie et al. 2017; Fu et al. 2013). In the following, we focus on the methods implemented in the reference SAMs used in this work.

GAEA relies on the observed relation between $R_{\text{mol}}(r)$ and the mid-plane pressure acting on the galactic disc $P_{\text{ext}}(r)$, assuming it applies at all redshifts (Blitz & Rosolowsky 2006).

$$R_{\text{mol}}(r) = \left(\frac{P_{\text{ext}}(r)}{P_0}\right)^\alpha \quad (8)$$

where P_0 is the external pressure of molecular clumps, and

$$P_{\text{ext}}(r) = \frac{\pi}{2} G \Sigma_{\text{g}}(r) [\Sigma_{\text{g}}(r) + f_{\sigma}(r) \Sigma_{\star, \text{d}}(r)] \quad (9)$$

In the previous equation, $f_{\sigma}(r) = \sigma_{\text{g}}(r)/\sigma_{\star, \text{d}}(r)$ is the ratio of the velocity dispersion profiles in the stellar and cold gas discs. The cold gas velocity dispersion in the disc is assumed to be constant, such that $\sigma_{\text{g}}(r) \equiv \sigma_{\text{g}} = 10 \text{ km s}^{-1}$, while that of the stellar disc is modelled as $\sigma_{\star, \text{d}}(r) = \sqrt{\pi G h_{\star} \Sigma_{\star, \text{d}}(r)}$ with $h_{\star} = r_{\star, \text{d}}/7.3$ (Xie et al. 2017).

L-Galaxies uses the modelling framework described in McKee & Krumholz (2010). In this case, the molecular fractions depends on

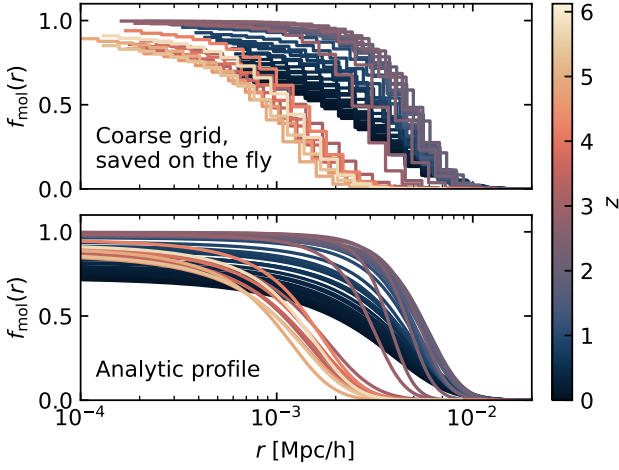


Figure 1. Example of the molecular hydrogen fraction profile $f_{\text{mol}}(r)$ for a GAEA model galaxy as a function of redshift. *Upper panel:* $f_{\text{mol}}(r)$ as output by the GAEA (De Lucia et al. 2024) SAM, where the hydrogen partition is explicitly computed with the Blitz & Rosolowsky (2006) prescription at every time step and saved on the fly for a predefined number of radial bins. *Lower panel:* $f_{\text{mol}}(r)$ re-evaluated on an arbitrarily smoother scale in post-processing with the Blitz & Rosolowsky (2006) prescription at each redshift snapshot.

cold gas surface density and metallicity.

$$f_{\text{mol}}(r) = \begin{cases} \frac{2[2-s]}{4+s} & s < 2 \\ 0 & s \geq 2 \end{cases}; \quad s(r) = \frac{\ln(1 + 0.6\chi + 0.01\chi^2)}{0.6\tau_c(r)} \quad (10)$$

$$\chi = \frac{3.1}{4.1} \left(1 + 3.1Z'^{0.365}\right); \quad \tau_c(r) = 0.066Z' \cdot (c_f \Sigma_g(r)) \quad (11)$$

where Z' is the gas-phase metallicity in solar units and c_f is the clumping factor, for which it is assumed (Henriques et al. 2020):

$$c_f = \begin{cases} 0.01^{-0.7} & Z' < 0.01 \\ Z'^{-0.7} & 0.01 \leq Z' < 1 \\ 1 & Z' \geq 1 \end{cases} \quad (12)$$

Both GAEA and L-Galaxies compute partitions and save the relevant information at each snapshot, for a predefined number of radial bins. The resulting total fraction f_{mol} (respectively ratio R_{mol}), i.e. over the total disc mass, is also saved.

Crucially, to have control over the radial resolution of surface density profiles, hence ultimately over that of our emission line model, we explicitly implement both Blitz & Rosolowsky (2006) and McKee & Krumholz (2010) prescriptions in post-processing of our reference SAMs outputs. Indeed, while the internal hydrogen partition schemes in both GAEA and L-Galaxies are computed on coarse radial grids (of the order of 20 bins), which is sufficient to derive star formation dynamics and associated processes, our specific objective, modelling the emission line, requires a finer resolution. By mirroring the internal hydrogen partition schemes of both SAMs, our approach thus allows to re-evaluate the profile on an arbitrarily smoother scale while maintaining consistency with respect to the stellar disc and gas disc properties we use as inputs. In other words, by reproducing the partition schemes analytically, we are able to evaluate them with high resolution in post-processing.

An example is presented in Figure 1, where the partition’s redshift evolution for a simulated galaxy from GAEA’s output is compared between the coarsely binned partition used internally and saved on

the fly, and the corresponding analytic profile (Blitz & Rosolowsky 2006), re-evaluated a posteriori on each snapshot.

3.2.2 Neutral hydrogen circular velocity profile

To model circular velocity profiles traced by the H I content, we assume the disc of model galaxies to be rotationally supported. Thus, the kinematics are closely tied to the gravitational potential in the disc plane. The potential is readily modelled from combining the mass distributions of the DM halo, stellar bulge, stellar disc and gas disc.

Here, we make the additional assumption that DM halos and stellar bulges have spherically symmetric profiles. Since our primary aim is ultimately to predict statistics over observable properties of rotationally-supported H I-rich systems, this assumption implies that we are modelling the average radial distributions across galaxy populations. In this context, asymmetries introduce noise around the average, which can be treated independently (see section 3.4).

In the Newtonian limit, the gravitational potential yields circular velocities

$$v_c(r) = \sqrt{\frac{GM(<r)}{r}} \quad (13)$$

where G is the gravitational constant and $M(<r)$ the total mass inside a radius r in galactocentric coordinates.

For dark matter halos, we follow the modelling of Obreschkow et al. (2009a) that we summarize below. We assume a Navarro-Frenk-White (Navarro et al. 1996) spherically symmetric profile.

$$\rho_h(r) = \rho_0 \left[\frac{r}{r_s} \left(1 + \frac{r}{r_s}\right)^2 \right]^{-1} \quad (14)$$

where ρ_0 is a normalisation factor and r_s is the characteristic scale radius of the halo. We then obtain the total mass profile by integrating over the density inside a sphere of radius r .

$$M_h(<r) = 4\pi \int_0^r d\tilde{r} \tilde{r}^2 \rho_h(\tilde{r}) \quad (15)$$

$$= 4\pi r_s^3 \rho_0 \left[\ln\left(1 + \frac{r}{r_s}\right) - \frac{r/r_s}{1 + r/r_s} \right] \quad (16)$$

The normalization factor ρ_0 is expressed in terms of the virial mass M_{vir} and virial radius r_{vir} by using the fact that $M_{\text{vir}} = M_h(<r_{\text{vir}})$.

$$\rho_0 = \frac{M_{\text{vir}}}{4\pi r_s^3} \cdot \left[\ln\left(1 + \frac{r_{\text{vir}}}{r_s}\right) - \frac{r_{\text{vir}}/r_s}{1 + r_{\text{vir}}/r_s} \right]^{-1} \quad (17)$$

By introducing the halo concentration parameter $c_h = r_{\text{vir}}/r_s$, the characteristic scale r_s is also expressed in terms of virial quantities. Following Obreschkow et al. (2009a), we assume a power law

$$c_h = \frac{12.3}{1+z} \left(\frac{M_{\text{vir}}}{1.3 \cdot 10^{13} h^{-1} M_\odot} \right)^{-0.13} \quad (18)$$

using the parameter tuning from Hennawi et al. (2007) consistent with empirical values derived from X-ray measurements and strong lensing data (Comerford & Natarajan 2007).

We model the stellar bulge with a Hernquist (Hernquist 1990) spherically symmetric profile.

$$\rho_{\star,b}(r) = \frac{M_{\star,b}}{2\pi} \frac{r_{\star,b}/r}{(r_{\star,b} + r)^3} \quad (19)$$

The total mass profile is again obtained by integrating over the density

inside a sphere of radius r .

$$M_{\star,b}(< r) = 4\pi \int_0^r d\tilde{r} \tilde{r}^2 \rho_{\star,b}(\tilde{r}) \quad (20)$$

$$= M_{\star,b} \left[\frac{r}{r_{\star,b} + r} \right]^2 \quad (21)$$

$$= M_{\star,b} \left[\frac{r}{r_{\star,b}} \cdot \frac{1}{1 + r/r_{\star,b}} \right]^2 \quad (22)$$

At last, for the stellar and cold gas discs, the gravitational potential in the equatorial plane of a disc with axially symmetric exponential surface density profile can be integrated analytically (Freeman 1970; Binney & Tremaine 2008), yielding circular velocity contributions of the following form.

$$v_{c,d}^2(r) = \frac{2GM_d}{r_d} y^2 [I_0(y)K_0(y) - I_1(y)K_1(y)] ; y = \frac{r}{2r_d} \quad (23)$$

where I_n and K_n are the modified Bessel functions of the first, respectively second kind.

The total circular velocity profile is obtained by generalizing eq. 13 as a quadrature rule, summing the squared contribution of each component.

$$v_c^2(r) = \sum_i v_{c,i}^2(r) \quad (24)$$

3.3 Model line profile

The normalised line profile $\Psi_{H1}(V)$ (as defined in section 3.1) is modelled through integration of the H1 disc's projected velocity field, weighted by its H1 surface density, onto the line of sight of an observer. Thanks to symmetry assumptions, this reduces to a radial integration

$$\Psi_{H1}(V) = \frac{\int_0^\infty dr r \Sigma_{H1}(r) \cdot \psi(V, r)}{\int_0^\infty dr r \Sigma_{H1}(r)} \quad (25)$$

where $\psi(V, r)$ is the line of sight velocity distribution (LOSVD) yielded by a thin ring portion of the disc at radius r , normalised such that $\int_V \psi(V, r) dV = 1 \forall r$, and with the denominator ensuring the normalization condition, $\int_V dV \Psi_{H1}(V) = 1$.

The LOSVD, in the rest frame of the system, can be derived from geometrical considerations (e.g. Obreschkow et al. 2009a).

$$\tilde{\psi}(V, r) = \begin{cases} \frac{1}{\pi} [(v_c(r) \sin i)^2 - V^2]^{-\frac{1}{2}} & \text{if } |V| < v_c(r) \sin i \\ 0 & \text{if } |V| \geq v_c(r) \sin i \end{cases} \quad (26)$$

where i is the inclination angle between the line of sight and the galactic plane's rotational axis, i.e. $i = 0$ when the galaxy is viewed 'face-on' and $i = \pi/2$ when it is 'edge-on'. In the following, for brevity, we do not write the inclination dependency explicitly.

This construction generates singular artifacts in the limit $V \rightarrow v_c(r) \sin i$, which are resolved by taking into account the effect of velocity dispersion. This is done by convolving the LOSVD of each thin ring with a gaussian kernel, preserving the normalization. In line with the assumptions made for the hydrogen partition (i.e. in eq. 9), we assume a fixed dispersion $\sigma_g \equiv 10 \text{ km s}^{-1}$ in the gas disc, leading to:

$$\psi(V, r) = \frac{1}{\sqrt{2\pi\sigma_g^2}} \int dV' \exp \left[\frac{(V - V')^2}{-2\sigma_g^2} \right] \cdot \tilde{\psi}(V', r) \quad (27)$$

Finally, the LOSVD of the disc can be combined by integrating over the infinitesimal radial contributions. The normalised H1 flux density is then obtained by weighting each thin ring by the surface density $\Sigma_{H1}(r)$.

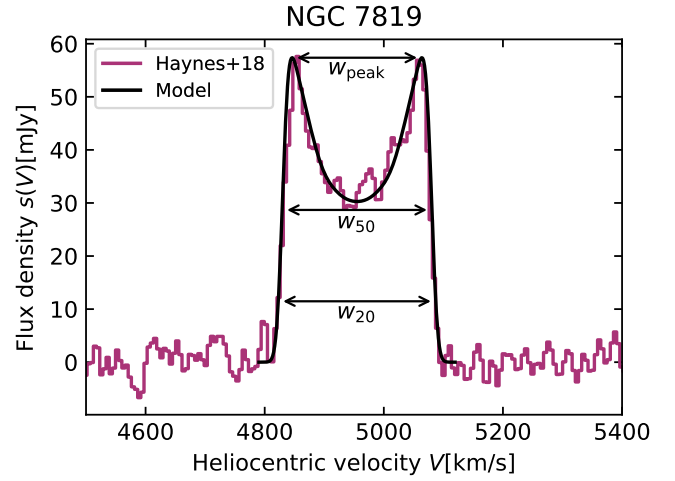


Figure 2. H I 21cm line profile of galaxy NGC 7819 measured in the ALFALFA survey (Haynes et al. 2018) (magenta curve), and a manual fit of our model as an example (black curve), displaying the model line width parameters, namely w_{peak} , w_{50} and w_{20} .

3.3.1 Emission line parametrisation

In observational studies, the information contained in the shape of the normalised line profile $\Psi_{H1}(V)$, and equivalently in that of the rest-frame flux density $s(V)$, is commonly parametrized by measurements of their widths, typically at the peak (w_{peak}), at 50% of the peak (w_{50}), and at 20% of the peak (w_{20}). While observationally these measurements pose definition and robustness challenges, the rest-frame symmetry in our model simplifies the derivation by ensuring that these quantities are always well-defined. As an example, Figure 2 shows the 21cm line profile of galaxy NGC 7819 as measured in the ALFALFA survey (Haynes et al. 2018), to which we fit our emission line model (eq. 1) by manually tuning the parameters, i.e. those from the set $\{M_{\text{vir}}, M_{\star,b}, M_{\star,d}, M_g, M_H, R_{\text{vir}}, r_{\star,b}, r_{\star,d}, r_g, f_{\text{mol}}\}$ described at the start of section 3.2. We also show the line width parameters, namely w_{peak} , w_{50} and w_{20} .

3.4 Simulation and observational effects

To compare the predictions of our emission line model with observational data, we need to take into account various effects that arise from either modelling assumptions or observational effects. We examine and implement models for these effects in a modular fashion. This allows to take a forward-modelling approach on our prediction framework, i.e. to predict data at low levels of processing, essentially including controlled effects in the simulation. In the broader picture, this kind of control is crucial for simulation pipelines used in precision cosmology.

3.4.1 Integration limits

As per eq. 25, the model features a radial integration that, in practice, is computed over a finite range $[0, r_{\text{max}}]$. We find that choosing $r_{\text{max}} = 9 \cdot r_g$, where r_g is the gas disc scale length, is an appropriate limit beyond which the marginal contribution to the emission line profile becomes negligible. In the following, we adopt this setting as default.

3.4.2 Inclination

In observations, galactic discs are viewed at an inclination angle i , which we take into account in our geometrical construction of the LOSVD. For galactic discs observed ‘edge-on’, i.e. when $i = \pi/2$, the dominant contribution to the profile shape is the rotational motion, typically inducing double-peak such as in Figure 2. In the case of a galaxy observed ‘face-on’, i.e. when $i = 0$, the contribution from the rotational motion is completely suppressed and the remaining emission line spread is purely due to velocity dispersion in the cold gas disc. Visually, the effect of inclination is a shrinking of the distance between the double peaks, hence a shrinking of the line width, compared to the ‘edge-on’ case. Assuming that galaxy orientations are uniformly distributed on the unit sphere, the distribution of inclinations i in the sky is proportional to $\sin(i)$. Observational studies thus sometimes apply a $1/\sin i$ correction to their line width measurements. In our framework, we account for the presence of this correction in data we compare our predictions to by simply setting $i = \pi/2$. Vice-versa, when forward-modelling the effect, we assign uniform random orientations on the unit sphere to each model galactic disc. While we checked that the spin orientations of DM halos in the Millennium suite are indeed uniformly distributed, using those as proxies for discs orientations would produce identical effects on the galaxy population statistics of interest. Using random orientations thus allows limiting computational resources to the relevant part for our study and treating the inclination effect in a purely modular fashion.

3.4.3 Redshift

The effect of redshift on emission line profiles can conceptually be divided in two parts. First, it offsets the rest-frame emission line center according to the systemic relative motion with respect to the observer. Second, it also has a broadening effect on line profiles since it is, by construction, linearly dependent on frequency, hence the lower frequency tail of the profile is shifted more than the higher frequency tail. This broadening effect is sometimes corrected for in observational surveys (e.g. in Kourkchi et al. 2020, 2022) by dividing observed line widths by a factor $(1+z)$. As our model directly predicts line profiles in the observed galaxy’s rest frame, we can readily include the redshift broadening effect by applying the inverse correction, namely multiplying rest-frame line widths by a factor $(1+z)$, when forward-modelling uncorrected data.

4 SIMULATED H I GALAXY CATALOGUES

Before the framework can serve for cosmological forecasts, its predictions must be validated against existing data. To this end, we construct mock observational catalogues of H I galaxies and compare them with available survey measurements.

4.1 Snapshot catalogues

Snapshot galaxy catalogues outputted by SAMs provide idealised representations of the simulated system, in the sense that they are observer-independent. To compare predictions from these catalogues with observational estimates, the latter are typically corrected for observational effects. In the following, we define distinct catalogues, each based on $z = 0$ snapshots for combinations of underlying N -body simulation, i.e. MSI or MSII, and SAM, i.e. GAEA or L-Galaxies.

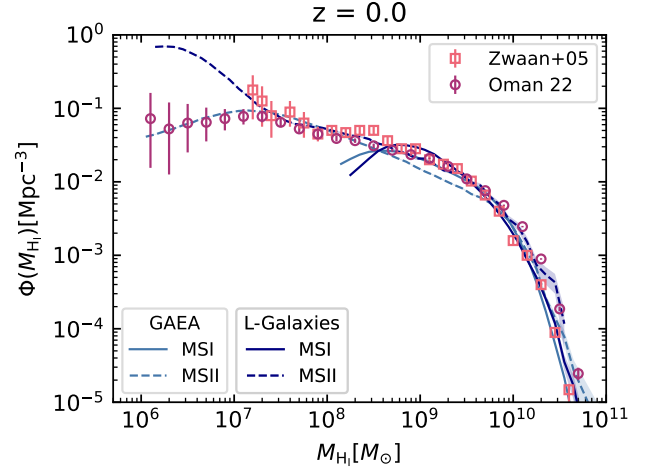


Figure 3. H I mass functions on $z = 0$ snapshot outputs. Blue lines correspond to GAEA outputs, and green lines to L-Galaxies outputs. Results are displayed for outputs from the MSI (solid lines), and MSII (dashed lines). These are compared to observational data derived from the HIPASS and ALFALFA surveys.

Accounting for their inherently finite resolution, it is expected that any simulation eventually becomes incomplete below a certain mass limit. Generally speaking, the resolution limits can only be accurately found by running the same physical model on a higher resolution simulation. For example, the MSII plays this role for the MSI. For our purpose, we want to study samples that are close to complete. The relevant portion of the catalogues thus sits above the completeness limit. In our snapshot catalogues, we fix conservative lower bounds in stellar and H I mass and discard the samples below. For catalogues based on the MSI, we set $M_{\star}, M_{\text{H I}} > 8.61 \cdot 10^7 M_{\odot}/h$. For those based on the MSII, we set $M_{\star}, M_{\text{H I}} > 6.88 \cdot 10^5 M_{\odot}/h$.

Further, we define the concept of ‘equi-representative’ random subsets for each snapshot catalogue, constructed by thinly binning the data in H I mass, and randomly selecting the same number of samples from each bin. We use these subsets to study scaling relations in the following (section 4.1.3).

4.1.1 Mass functions

The local ($z \approx 0$) H I mass function is used to calibrate both GAEA and L-Galaxies (observational data from the HIPASS survey (Zwaan et al. 2005) are used as a reference in both cases). Figure 3 shows how the snapshot catalogues, by construction, thus reproduce these data as well as more recent ones from the ALFALFA survey. Specifically, we consider here a reanalysis by Oman (2022). It is important to remember that, on the observational data side, the H I mass function is obtained through volume/density estimation techniques that typically factor in (in)completeness effects, the uncertainties of which become larger in the lower mass end.

4.1.2 Velocity/Width functions

Using our emission line model, we investigate the ‘width functions’ (WF) obtained for each catalogue, i.e. the volume-normalised distribution of emission line widths. This quantity essentially probes an observable equivalent to the velocity function (VF), using 21cm line widths as a proxy for circular velocities instead of e.g. v_{max} . We note

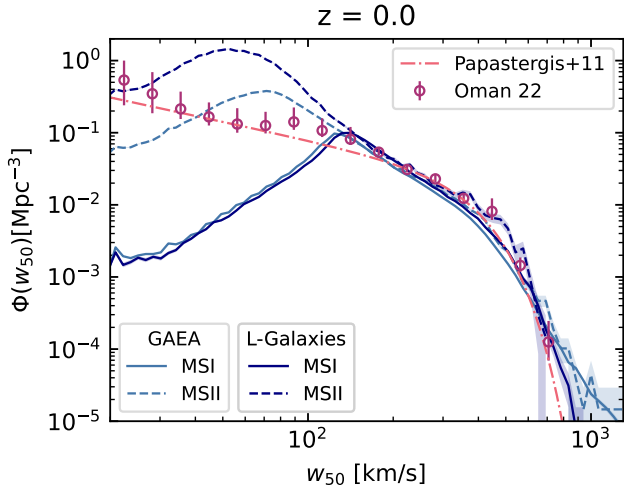


Figure 4. H I velocity width (w_{50}) functions on $z = 0$ snapshot outputs. Blue lines correspond to GAEA outputs, and green lines to L-Galaxies outputs. Results are displayed for outputs from the MSI (solid lines), and MSII (dashed lines). These are compared to observational data derived from the (40% and 100% releases of the) ALFALFA survey.

that while the H I mass function considered in the previous section was used to fine tune model parameters, the width function considered here is a real prediction of our simulations. Figure 4 shows the w_{50} -functions derived from GAEA and L-Galaxies snapshots at $z = 0$ compared to those derived from ALFALFA 40% (Papastergis et al. 2011) and ALFALFA 100% data (reanalysis by Oman 2022). The observational estimates shown in this figure are not corrected for inclination nor for redshift effects. For proper comparison, we thus forward-model these effects on our predictions (as described in sections 3.4.2 and 3.4.3). While the knee and larger widths parts of the distribution match observational data relatively well, some significant differences are evident in the lower velocity end. First, the completeness limits of the SAM samples are visible where the width functions peak and then decline towards lower velocity width. Second, in the range between the completeness limit and the ‘knee’ of the width function, the predicted slopes are higher than those observed. This mismatch was already reported in Papastergis et al. (2011). The study of Chauhan et al. (2019) found similar predictions for the SHARK SAM and showed that forward-modelling selection effects allows model predictions to be reconciled with observations. In addition, Oman (2022) showed that a significant selection bias may be associated to the volume/density estimators used in observational studies.

4.1.3 Scaling relations

Both the H I mass functions and the width functions may be thought of as proportional to marginal distributions of higher dimensional scaling relations between galaxy properties. For example, up to a volume normalisation, the generalised Tully-Fisher relation between $M_{\text{H I}}$ and w_{50} represents a 2D distribution of which the H I mass function and H I width function are marginal distributions.

Figure 5 shows generalised Tully-Fisher scaling relations between stellar, baryonic, and H I masses and edge-on peak line widths, obtained using the equi-representative subsets (see section 4.1) at $z = 0$. We show the 67% and 95% confidence level contours of the distribu-

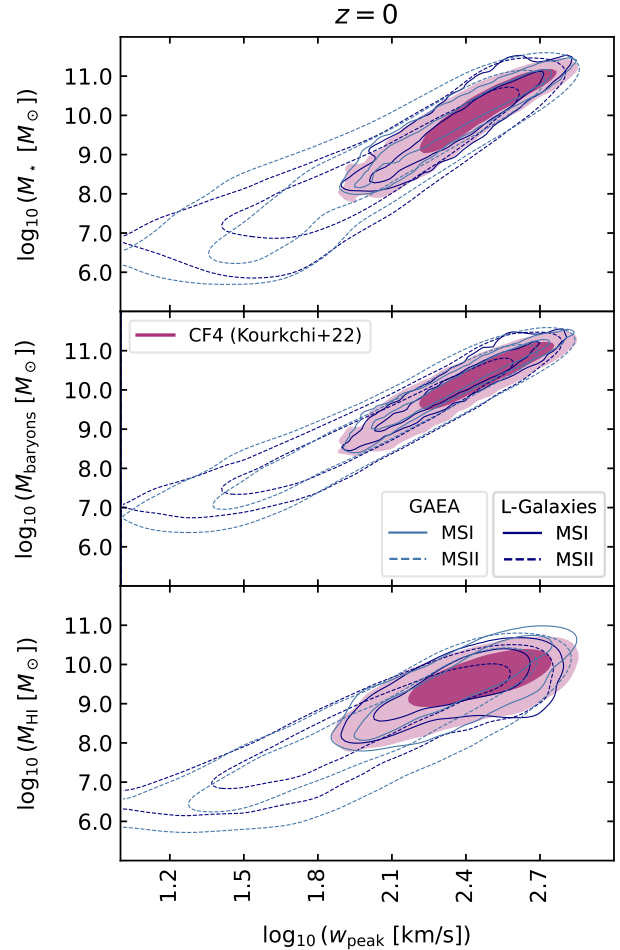


Figure 5. Generalised Tully-Fisher relations between edge-on peak line widths (w_{peak}) and stellar, baryonic, and H I masses on $z = 0$ snapshot outputs. Contours show the 67% and 95% confidence levels of sample distributions for each simulation, namely the GAEA (blue) MSI (solid), MSII (dashed), and L-Galaxies (green) MSI (solid), MSII (dashed). Magenta contours present distributions derived from CosmicFlows 4 baryonic Tully-Fisher catalogue’s data (Kourkchi et al. 2022).

tions for GAEA and L-Galaxies outputs based on MSI and MSII. The subset catalogues, representing $\sim 10^4$ simulated galaxies each, are compared to observational data from the CosmicFlows 4 (hereafter CF4) bTFR catalogue (Kourkchi et al. 2022). The CF4 catalogue is the result of a broad combination of observations from multiple instruments at various frequencies, and the data are corrected for inclination, redshift and instrumental effects. Their linewidth parametrization W_{mx} (see Courtois et al. 2009, 2011) is defined as ‘statistically descriptive of the peak-to-peak maximum rotation velocity of a galaxy’, i.e. is a proxy of w_{peak} .

Figure 6 presents the predicted redshift evolution of the generalised Tully-Fisher scaling relations between stellar, baryonic, and H I masses and edge-on peak line widths, obtained using our equi-representative subsets (see section 4.1) at redshift $0 < z < 3$. The 67% and 95% confidence level contours of the distributions are displayed for GAEA outputs based on the MSI (solid) and MSII (dashed). Our simulations predict that the principal effect of redshift evolution is

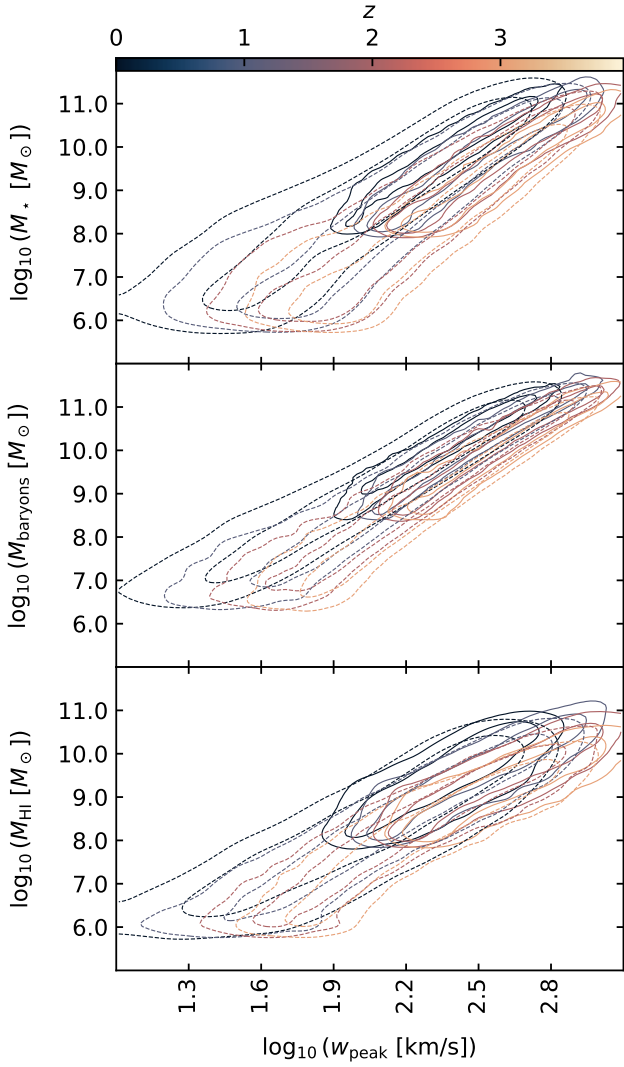


Figure 6. Generalised Tully-Fisher relations between edge-on peak line widths (w_{peak}) and stellar, baryonic, and H I masses on snapshot outputs at redshifts $0 < z < 3$. Contours show the 67% and 95% confidence levels of sample distributions obtained from the GAEA MSI (solid), and GAEA MSII (dashed) catalogues.

an offset of the relations towards higher widths, while the slope and scatter remain stable.

4.2 Light-cone catalogues

From GAEA MSI snapshot outputs we construct mock survey catalogues, projecting and redshifting model galaxies on light-cones, using the framework presented in [Blaizot et al. \(2005\)](#) and [Zoldan et al. \(2017\)](#). In particular, we define two geometries: the first one, which we use hereafter to simulate the ALFALFA survey with $z < 0.06$; and the second one, which we use in section 6 to forecast a SKAO H I galaxy survey with $z < 0.4$. The corresponding solid angles covered by the simulated light-cones are constrained by the size of the MSI. We obtain $\Omega \approx 5230 \text{ deg}^2$ for our mock ALFALFA light-cone, and $\Omega \approx 500 \text{ deg}^2$ for our mock SKAO light-cone.

4.2.1 Selection function

To model the selection function, we define masks for sensitivity limits and apply them to the light-cone catalogues. Specifically, to compare our first light-cone with data from the ALFALFA survey ([Haynes et al. 2018](#)), we adopt their specified 5σ survey sensitivity (in terms of velocity-integrated flux): $0.72 \text{ Jy km s}^{-1}$ for $w_{50} = 200 \text{ km s}^{-1}$, which we translate into a $720 \text{ mJy km s}^{-1} / 200 \text{ km s}^{-1} = 3.6 \text{ mJy}$ threshold on peak flux density. This approximation is reasonable as the mode of the observed distribution of line widths in the ALFALFA sample ([Haynes et al. 2018](#)) is around $w_{50} \approx 200 \text{ km s}^{-1}$.

4.2.2 Redshift distribution

Figure 7 shows the redshift distribution of H I galaxies for our mock ALFALFA catalogue compared to the real ALFALFA data. The visible dips in the real data at $z \sim 0.019, 0.029$ and 0.052 correspond to the effect of radio frequency interference ([Haynes et al. 2018](#)), which we do not try to reproduce.

We note that the mock ALFALFA light-cone suffers from the same simulation resolution limits discussed above for the snapshot catalogues. The incompleteness at low H I masses translates in an underprediction of the number counts below $z \lesssim 0.01$, where real observational sensitivity allows the detection of galaxies with lower H I mass. Hence, the predicted dN/dz should be interpreted as a lower bound in the very local regime. This is also a regime where the sampled volume is small and thus the signal is more sensitive to cosmic variance.

The dN/dz distribution, normalised by the solid angle Ω spanned by the survey area, is well described by an exponentially damped power law parametrization (e.g. [Obreschkow et al. 2009b](#)).

$$\frac{dN}{dz} \approx 10^{c_1} z^{c_2} \exp(-c_3 z) \quad (28)$$

Figure 7 shows the best fit of this parametrization for our mock catalogue, with parameters: $c_1 = 8.37$, $c_2 = 3.07$, $c_3 = 121.77$. The resulting curve can be integrated over the redshift range to estimate the average number of galaxies detected per square degree of survey sky.

$$N(z < z_{\text{max}}) / \text{deg}^2 = \int_0^{z_{\text{max}}} [10^{c_1} z^{c_2} \exp(-z c_3)] dz \quad (29)$$

$$= \frac{10^{c_1}}{c_3^{c_2+1}} \gamma(c_2 + 1, z_{\text{max}} c_3) \quad (30)$$

where $\gamma(s, x)$ is the lower incomplete gamma function. In Figure 7, this method is employed to derive an estimate for the mock ALFALFA sample.

4.2.3 Mass and width distributions on the light-cone

In contrast with results obtained in sections 4.1.1 and 4.1.2 that rely on corrections to observational estimates, we can leverage our forward-modelled selection function to analyse predictions closer to the direct observables, namely probing the observable H I mass and line width distributions on the light-cones. We follow the approach of [Chauhan et al. \(2019\)](#), and normalise by the survey area, i.e. the solid angle Ω described by the light-cone's sky coverage. For ALFALFA data, we use $\Omega = 7000 \text{ deg}^2$. Figures 8 and 9 show the resulting mass and width distributions for our mock ALFALFA catalogue, compared to those from the ALFALFA survey. Since the data are uncorrected for any effect, we forward-model the effect of inclination and redshift in our predictions (as described in sections 3.4.2 and 3.4.3). The

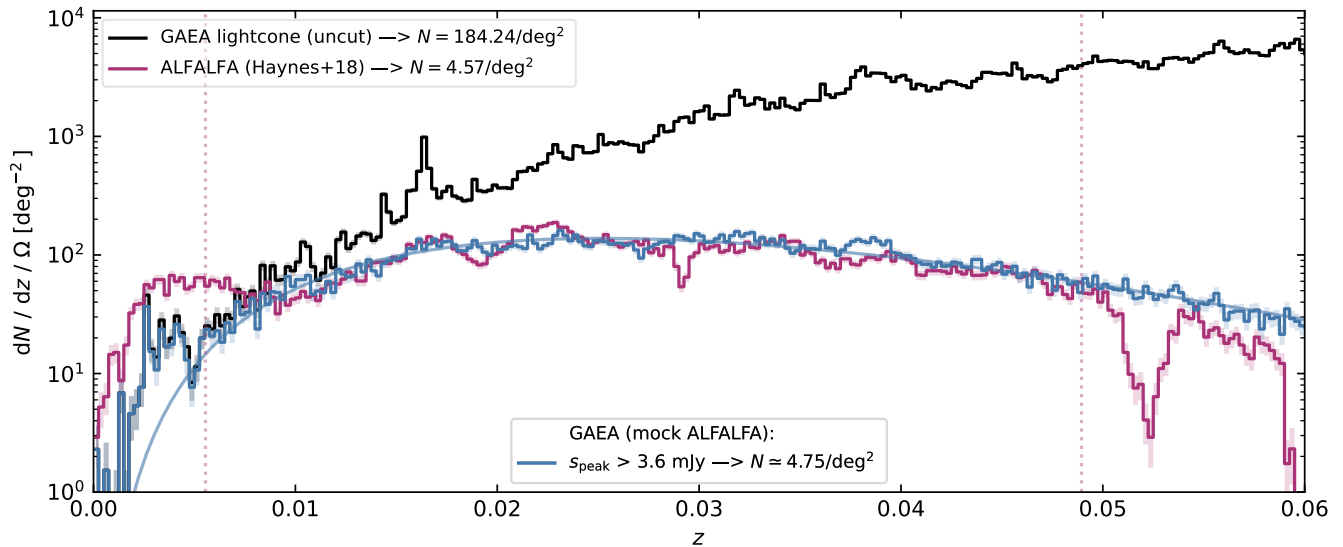


Figure 7. Redshift distribution of H I galaxy samples, normalized by survey area Ω . The black histogram shows the the uncut GAEA light-cone, i.e. before applying any selection. The blue histogram shows the sample obtained by applying a peak flux density limit $s_{\text{peak}} > 3.6$ mJy. The blue curve shows the best fit estimate to the mock ALFALFA sample for the The magenta histogram shows real data from the ALFALFA survey (Haynes et al. 2018). Dotted vertical lines highlight the 0.05 and 0.95 percentiles of the observational data’s redshift distribution. For all samples, we derive the average number of galaxies detected (in the range $0 < z < 0.06$) per square degree of survey sky.

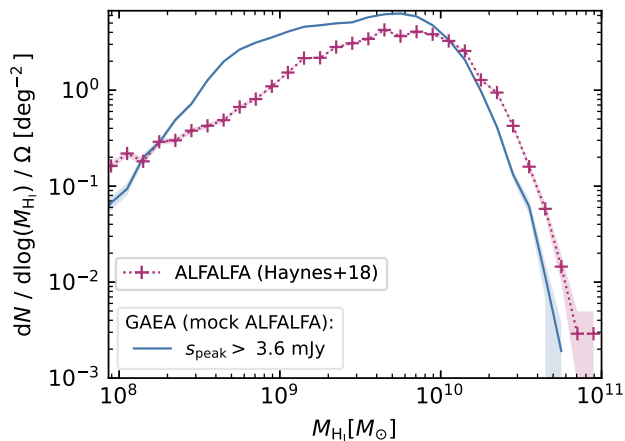


Figure 8. Observable H I mass distributions on the light-cone, normalised by survey area. The blue curve corresponds to the GAEA mock ALFALFA catalogue obtained with a peak flux density cut. The dotted magenta curve shows, for comparison, the H I mass distribution of real ALFALFA catalogue (Haynes et al. 2018).

predicted distributions shapes match observational measurements well. Similar results were obtained by Chauhan et al. (2019), with an even closer level of agreement. A source of difference might reside at the N-body simulations level, as they use the SURFS suite which has smaller volumes and sharper mass resolution than the Millennium suite.

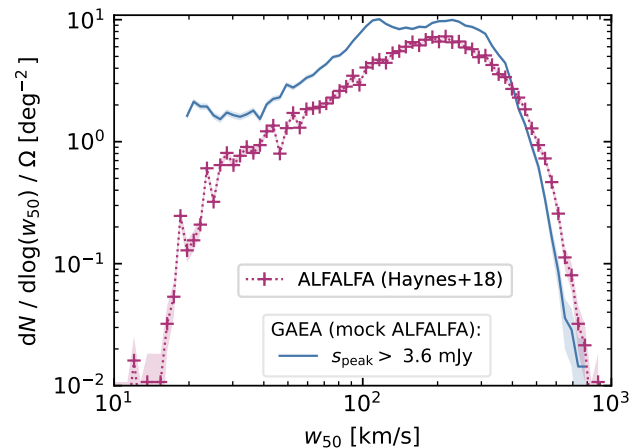


Figure 9. Observable width (w_{50}) distributions on the light-cone, normalised by survey area. The blue curve corresponds to the GAEA mock ALFALFA catalogue obtained with a peak flux density cut. The dotted magenta curve shows, for comparison, the width (w_{50}) distribution of the real ALFALFA catalogue (Haynes et al. 2018).

4.2.4 Scaling relations on the light-cone

Much like in section 4.1.3, the H I mass and width distributions may be thought of as marginal distributions of higher dimensional relations. Leveraging our forward-model of the selection function, and redshift effects, we compare predictions for those higher dimensional relations directly with observational data from the ALFALFA survey catalogue (Haynes et al. 2018). Figure 10 shows this comparison for the generalized Tully-Fisher scaling relation between line widths (w_{50}) and H I masses.

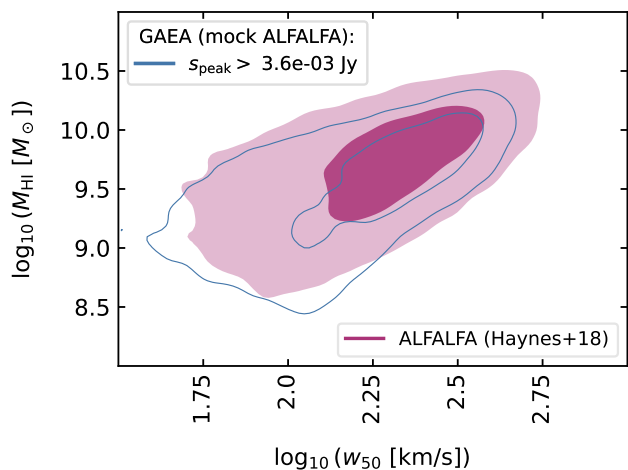


Figure 10. Scaling relation between galaxy line widths (w_{50}) and galaxy H I masses. Contours show the 67% and 95% confidence levels of samples distributions. Blue contours correspond to the GAEA "mock ALFALFA" sample catalogue obtained with a peak flux density cut. Magenta contours correspond to the raw distribution from the ALFALFA survey catalogue (Haynes et al. 2018), uncorrected for inclination and redshift effects.

5 DISCUSSION

The initial and most fundamental test of our 21 cm emission line simulations is their ability to reproduce empirical results derived from local Universe observations. Results presented in Section 4.1, in particular in figure 5, suggest a solid match between observational constraints and our predictions for the width function and generalized Tully-Fisher relations. This consistency is not a trivial outcome and serves as an independent validation of the physical prescriptions within both our model and semi-analytical models. Consistency of these predictions between GAEA and L-Galaxies further reinforces this result, suggesting that our framework captures the essential physics governing the internal dynamics of H I galaxies in the local Universe.

Inspection of the width function reveals both the successes and limitations of modelling at the level of snapshots. While the knee and high-width portions of the distribution match observational data well, the predicted slopes in the low-width regime are steeper than observed. This discrepancy, previously reported by Papastergis et al. (2011), likely arises from selection biases in observational samples. Chauhan et al. (2019) demonstrated that forward-modelling selection effects can largely reconcile such predictions with observations, and Oman (2022) showed that volume/density estimators used in deriving observational width functions introduce significant biases. Our results are consistent with these findings, reinforcing the interpretation that the intrinsic width function slope may indeed be steeper than current observational estimates suggest.

Looking at predictions for snapshots at higher redshifts (Figure 6), the redshift evolution shows a clear trend where generalized Tully-Fisher relations, at fixed mass, are offset towards broader linewidths with increasing redshift. Obreschkow et al. (2009a) argued that this is a consequence of the ‘mass-radius-velocity relation’ for dark matter haloes in the Millennium simulations (Croton et al. 2006; Mo et al. 1998), which assumes, for a fixed halo mass, a scaling of the circular velocity v_c asymptotically proportional to $\sqrt{1+z}$. Whether this predicted evolution is fully physical or partly an artifact of the simulation assumptions thus remains to be tested.

Table 1. Best-fit parameters for model $dN/dz/\Omega$ (eq. 28) on mock SKAO H I galaxy surveys ($0 < z < 0.4$) for a range of spectral sensitivities.

	c_1	c_2	c_3
$s_{\text{peak}} > 10^{-6}\text{Jy}$	6.32	2.09	3.11
$s_{\text{peak}} > 10^{-5}\text{Jy}$	6.55	2.21	7.06
$s_{\text{peak}} > 10^{-4}\text{Jy}$	6.87	2.34	20.19
$s_{\text{peak}} > 10^{-3}\text{Jy}$	6.49	2.05	55.73
$s_{\text{peak}} > 10^{-2}\text{Jy}$	6.53	2.02	175.54

Completing our model with light-cone projection, inclination, redshift and selection effects, we find that peak flux density limits on our mock ALFALFA light-cone allow to reproduce the redshift distribution (Figure 7), H I scaling relations (Figures 10) and respective marginal distributions (Figures 8, 9) of uncorrected observational data from the ALFALFA survey (Haynes et al. 2018). We note that the level of agreement of similar results reported by Chauhan et al. (2019) using the SHARK SAM and SURFS simulation suite is higher than that obtained here. This difference may arise from variations in the volume and resolution of the underlying dark matter simulation employed, or in the treatment of selection effects. The consistency between our GAEA and L-Galaxies predictions, despite their distinct semi-analytic prescriptions and underlying cosmologies, is a standalone result. It provides evidence that the H I line predictions are robust to the choice of semi-analytic galaxy formation model, a necessary condition for trusting them as tools for survey forecasting and cosmological inference.

6 FORECAST FOR A SKAO H I GALAXY SURVEY

Considering the good level of agreement shown between model predictions and existing data, we investigate forecasts for future SKAO H I galaxy surveys with our second light-cone catalogue. A basic and important quantity to consider is the expected number counts at different cosmic epochs, as a function of sensitivity. We compute the dN/dz functions for a logarithmically spaced range of peak flux density limits, between $1 \mu\text{Jy}$ and 10mJy . Figure 11 shows the results obtained, where, for all samples, we derive the corresponding average number of galaxies (in the range $0 < z < 0.4$) per square degree of survey sky. For the raw light-cone, i.e. before applying selection cuts, this is obtained by dividing the total number of galaxies in the catalogue by the survey area. For mock H I surveys, we fit the parametric model (eq. 28) and find best fit parameters, which we report in table 1. The fitted curves are integrated over redshift (eq. 30) to estimate the number counts per square degree reported in the figure.

These forecasts demonstrate the dramatic dependence of number counts on instrumental sensitivity and can thus inform trade-offs between survey depth, area, and spectral resolution for the planning of future SKAO observations.

7 CONCLUSIONS

In this work, we have presented a modern framework to bridge outputs of the GAEA and L-Galaxies semi-analytical models to robust predictions for observables tied to the 21 cm emission line in H I-rich galaxies. The main conclusions of this study are summarized as follows:

(1) The model successfully reproduces key observational local Universe constraints that were not used in its calibration, including

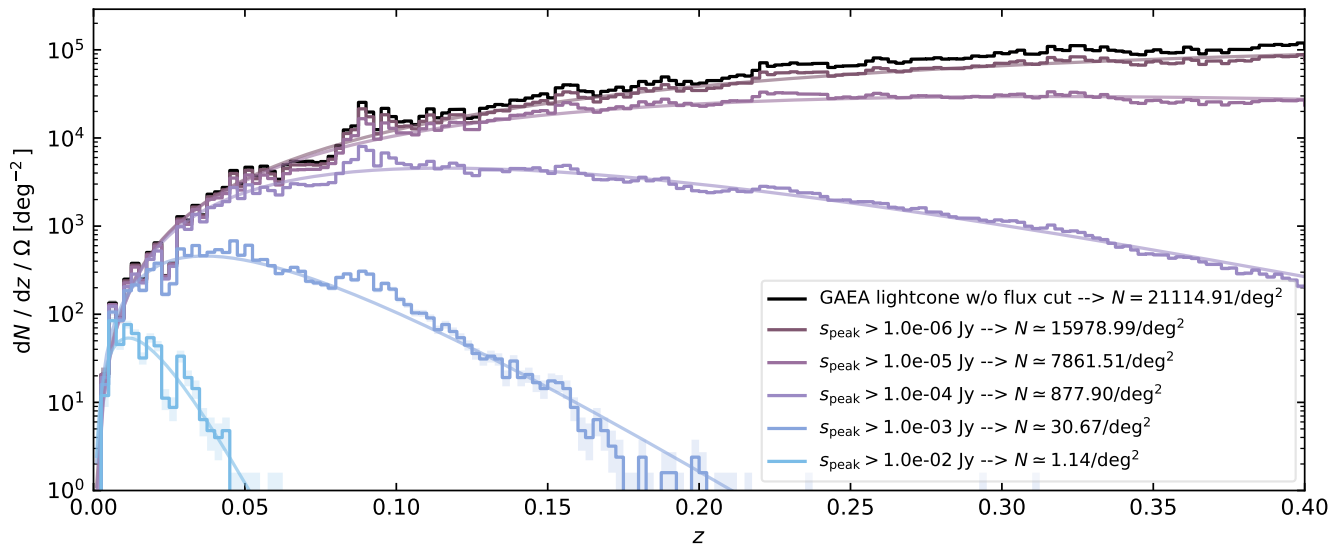


Figure 11. Redshift distribution of H I galaxies for GAEA mock SKAO observations, with a range of peak flux density thresholds covering orders of magnitudes in spectral sensitivities from tens of mJy to μ Jy. The black histogram shows the redshift distribution of the uncut GAEA projected light-cone, i.e. before applying any flux cut. Coloured histograms show the sub-samples obtained by applying the respective peak flux density detection limit to the mock catalogue.

generalized Tully-Fisher scaling relations and their marginal distributions.

(2) The model predictions are consistent between both underlying semi-analytic models tested, GAEA and L-Galaxies, reinforcing their mutual robustness.

(3) We generate mock light-cone catalogues that replicate the statistical distributions of H I-selected galaxies observed in the ALFALFA survey, demonstrating control over observational effects and selection-induced biases which are forward-modelled.

(4) We present forecasts for a H I galaxy redshift survey with the SKA Observatory and quantitative predictions for redshift distributions of galaxy number counts that highlight the crucial role of instrumental sensitivity.

As H I galaxy surveys with the SKAO move toward the statistical samples needed for precision cosmology, validated prediction frameworks such as the one presented in this work will become ever more indispensable. Indeed, the Tully-Fisher relation serves as a distance indicator, enabling peculiar velocity catalogues that probe the cosmic growth rate of structure, contribute to independent H_0 determinations, and test gravity at cosmological scales. Such cosmological probes have, historically, been limited by the data, i.e. by the samples sizes and redshift coverages. With the advent of the SKA Observatory, the scale of peculiar velocity measurements could turn them into powerful constraints on cosmological models. The framework presented in this work provides a controlled basis to build predictions of the precision and systematic uncertainties of such measurements.

ACKNOWLEDGEMENTS

This work was supported in part by grant CRSII5_193826 from the Swiss National Science Foundation, by the Swiss State Secretariat for Education, Research and Innovation (SERI) as part of the SKACH consortium, and by the French government through the France 2030 investment plan managed by the National Research Agency (ANR),

as part of the Initiative of Excellence Université Côte d’Azur under reference number ANR-15-IDEX-01.

DATA AND CODE AVAILABILITY

This work uses previously published data as referenced and described in the text. Details of the analysis and code can be made available upon reasonable request to the corresponding author.

REFERENCES

- Almeida A., et al., 2023, *ApJS*, **267**, 44
 Angulo R. E., Hilbert S., 2015, *MNRAS*, **448**, 364
 Angulo R. E., White S. D. M., 2010, *MNRAS*, **405**, 143
 Barnes D. G., et al., 2001, *MNRAS*, **322**, 486
 Baugh C. M., et al., 2019, *MNRAS*, **483**, 4922
 Begeman K. G., 1989, *A&A*, **223**, 47
 Bell E. F., de Jong R. S., 2001, *ApJ*, **550**, 212
 Bigiel F., Leroy A., Walter F., Brinks E., de Blok W. J. G., Madore B., Thornley M. D., 2008, *AJ*, **136**, 2846
 Binney J., Tremaine S., 2008, *Galactic Dynamics: Second Edition*. Princeton University Press
 Blaizot J., Wadadekar Y., Guiderdoni B., Colombi S. T., Bertin E., Bouchet F. R., Devriendt J. E. G., Hatton S., 2005, *MNRAS*, **360**, 159
 Blitz L., Rosolowsky E., 2006, *ApJ*, **650**, 933
 Blyth S., et al., 2016, in *MeerKAT Science: On the Pathway to the SKA*. p. 4, doi:10.22323/1.277.0004
 Boselli A., Gavazzi G., 2006, *PASP*, **118**, 517
 Boubel P., Colless M., Said K., Staveley-Smith L., 2024a, *MNRAS*, **531**, 84
 Boubel P., Colless M., Said K., Staveley-Smith L., 2024b, *MNRAS*, **533**, 1550
 Boubel P., Colless M., Said K., Staveley-Smith L., 2025, *J. Cosmology Astropart. Phys.*, **2025**, 066
 Boylan-Kolchin M., Springel V., White S. D. M., Jenkins A., Lemson G., 2009, *MNRAS*, **398**, 1150
 Braun R., Bonaldi A., Bourke T., Keane E., Wagg J., 2019, *arXiv e-prints*, p. arXiv:1912.12699

- Cantarella S., De Lucia G., Fontanot F., Hirschmann M., Xie L., Franco M., Plat A., 2025, [arXiv e-prints](#), p. [arXiv:2511.03787](#)
- Catinella B., et al., 2010, *MNRAS*, **403**, 683
- Chaikin E., et al., 2025, [arXiv e-prints](#), p. [arXiv:2509.04067](#)
- Chauhan G., Lagos C. d. P., Obreschkow D., Power C., Oman K., Elahi P. J., 2019, *MNRAS*, **488**, 5898
- Chen H., Xie L., Wang J., Hu W., De Lucia G., Fontanot F., Hirschmann M., 2024, *MNRAS*, **528**, 2451
- Colless M., et al., 2001, *MNRAS*, **328**, 1039
- Comerford J. M., Natarajan P., 2007, *MNRAS*, **379**, 190
- Cora S. A., et al., 2018, *MNRAS*, **479**, 2
- Cortese L., Catinella B., Janowiecki S., 2017, *ApJ*, **848**, L7
- Courtois H. M., Tully R. B., Fisher J. R., Bonhomme N., Zavodny M., Barnes A., 2009, *AJ*, **138**, 1938
- Courtois H. M., Tully R. B., Makarov D. I., Mitronova S., Koribalski B., Karachentsev I. D., Fisher J. R., 2011, *MNRAS*, **414**, 2005
- Croton D. J., et al., 2006, *MNRAS*, **365**, 11
- DESI Collaboration et al., 2016, [arXiv e-prints](#), p. [arXiv:1611.00036](#)
- DESI Collaboration et al., 2025, [arXiv e-prints](#), p. [arXiv:2503.14745](#)
- Davé R., Anglés-Alcázar D., Narayanan D., Li Q., Rafieferantsoa M. H., Appleby S., 2019, *MNRAS*, **486**, 2827
- Dawson K. S., et al., 2013, *AJ*, **145**, 10
- Dawson K. S., et al., 2016, *AJ*, **151**, 44
- De Lucia G., Blaizot J., 2007, *MNRAS*, **375**, 2
- De Lucia G., Tornatore L., Frenk C. S., Helmi A., Navarro J. F., White S. D. M., 2014, *MNRAS*, **445**, 970
- De Lucia G., Fontanot F., Xie L., Hirschmann M., 2024, *A&A*, **687**, A68
- Dekel A., Birnboim Y., 2006, *MNRAS*, **368**, 2
- Desmond H., 2012, [arXiv e-prints](#), p. [arXiv:1204.1497](#)
- Diemer B., et al., 2018, *ApJS*, **238**, 33
- Dubois Y., et al., 2021, *A&A*, **651**, A109
- Duffy A. R., Moss A., Staveley-Smith L., 2012a, *Publ. Astron. Soc. Australia*, **29**, 202
- Duffy A. R., Meyer M. J., Staveley-Smith L., Bernyk M., Croton D. J., Koribalski B. S., Gerstmann D., Westerlund S., 2012b, *MNRAS*, **426**, 3385
- Elahi P. J., Welker C., Power C., Lagos C. d. P., Robotham A. S. G., Cañas R., Poulton R., 2018, *MNRAS*, **475**, 5338
- Euclid Collaboration et al., 2024, *A&A*, **689**, A276
- Euclid Collaboration et al., 2025, *A&A*, **697**, A1
- Fernández X., et al., 2013, *ApJ*, **770**, L29
- Fernández X., et al., 2016, *ApJ*, **824**, L1
- Fontanot F., Hirschmann M., De Lucia G., 2017, *ApJ*, **842**, L14
- Fontanot F., et al., 2020, *MNRAS*, **496**, 3943
- Fontanot F., et al., 2021, *MNRAS*, **504**, 4481
- Fontanot F., De Lucia G., Xie L., Hirschmann M., Baugh C., Helly J. C., 2025, *A&A*, **699**, A108
- Fraternali F., Binney J. J., 2008, *MNRAS*, **386**, 935
- Freeman K. C., 1970, *ApJ*, **160**, 811
- Fu J., Guo Q., Kauffmann G., Krumholz M. R., 2010, *MNRAS*, **409**, 515
- Fu J., et al., 2013, *MNRAS*, **434**, 1531
- Giovanelli R., Haynes M. P., 1988, in Kellermann K. I., Verschuur G. L., eds., *Galactic and Extragalactic Radio Astronomy*. Springer-Verlag, pp 522–562
- Giovanelli R., et al., 2005, *AJ*, **130**, 2598
- Gnedin N. Y., Kravtsov A. V., 2011, *ApJ*, **728**, 88
- Gunn J. E., Gott III J. R., 1972, *ApJ*, **176**, 1
- Guo Q., et al., 2011, *MNRAS*, **413**, 101
- Haynes M. P., et al., 2011, *AJ*, **142**, 170
- Haynes M. P., et al., 2018, *ApJ*, **861**, 49
- Hennawi J. F., Dalal N., Bode P., Ostriker J. P., 2007, *ApJ*, **654**, 714
- Henriques B. M. B., White S. D. M., Thomas P. A., Angulo R., Guo Q., Lemson G., Springel V., Overzier R., 2015, *MNRAS*, **451**, 2663
- Henriques B. M. B., Yates R. M., Fu J., Guo Q., Kauffmann G., Srisawat C., Thomas P. A., White S. D. M., 2020, *MNRAS*, **491**, 5795
- Hernquist L., 1990, *ApJ*, **356**, 359
- Hirschmann M., De Lucia G., Fontanot F., 2016, *MNRAS*, **461**, 1760
- Hollenbach D., Salpeter E. E., 1971, *ApJ*, **163**, 155
- Howlett C., 2019, *MNRAS*, **487**, 5209
- Howlett C., Staveley-Smith L., Blake C., 2017, *MNRAS*, **464**, 2517
- Jarvis M., et al., 2016, in MeerKAT Science: On the Pathway to the SKA. p. 6 ([arXiv:1709.01901](#)), doi:10.22323/1.277.0006
- Jiang Z., Wang J., Gao L., Zhang F.-H., Guo Q., Wang L., Pan J., 2019, *Research in Astronomy and Astrophysics*, **19**, 151
- Johnston S., et al., 2008, *Experimental Astronomy*, **22**, 151
- Kennicutt R. C., Evans N. J., 2012, *ARA&A*, **50**, 531
- Kereš D., Katz N., Weinberg D. H., Davé R., 2005, *MNRAS*, **363**, 2
- Kerr F. J., Hindman J. F., Robinson B. J., 1954, *Australian Journal of Physics*, **7**, 297
- Koda J., et al., 2014, *MNRAS*, **445**, 4267
- Koribalski B. S., et al., 2020, *Ap&SS*, **365**, 118
- Kourkchi E., et al., 2020, *ApJ*, **902**, 145
- Kourkchi E., Tully R. B., Courtois H. M., Dupuy A., Guinet D., 2022, *MNRAS*, **511**, 6160
- Krumholz M. R., 2013, *MNRAS*, **436**, 2747
- Krumholz M. R., McKee C. F., Tumlinson J., 2009, *ApJ*, **699**, 850
- Lacey C. G., et al., 2016, *MNRAS*, **462**, 3854
- Lagos C. D. P., Baugh C. M., Lacey C. G., Benson A. J., Kim H.-S., Power C., 2011, *MNRAS*, **418**, 1649
- Lagos C. d. P., Tobar R. J., Robotham A. S. G., Obreschkow D., Mitchell P. D., Power C., Elahi P. J., 2018, *MNRAS*, **481**, 3573
- Laureijs R., et al., 2011, [arXiv e-prints](#), p. [arXiv:1110.3193](#)
- Lelli F., McGaugh S. S., Schombert J. M., 2016, *AJ*, **152**, 157
- Lelli F., McGaugh S. S., Schombert J. M., Desmond H., Katz H., 2019, *MNRAS*, **484**, 3267
- Maddox N., et al., 2021, *A&A*, **646**, A35
- McCarthy I. G., Schaye J., Bird S., Le Brun A. M. C., 2017, *MNRAS*, **465**, 2936
- McGaugh S. S., 2005, *ApJ*, **632**, 859
- McGaugh S. S., Schombert J. M., Bothun G. D., de Blok W. J. G., 2000, *ApJ*, **533**, L99
- McKee C. F., Krumholz M. R., 2010, *ApJ*, **709**, 308
- Meyer M. J., et al., 2004, *MNRAS*, **350**, 1195
- Mo H. J., Mao S., White S. D. M., 1998, *MNRAS*, **295**, 319
- Murphy E. J., et al., 2018, in Murphy E., ed., *Astronomical Society of the Pacific Conference Series Vol. 517, Science with a Next Generation Very Large Array*. p. 3 ([arXiv:1810.07524](#)), doi:10.48550/arXiv.1810.07524
- Navarro J. F., Frenk C. S., White S. D. M., 1996, *ApJ*, **462**, 563
- Obreschkow D., Croton D., De Lucia G., Khochfar S., Rawlings S., 2009a, *ApJ*, **698**, 1467
- Obreschkow D., Klöckner H.-R., Heywood I., Levrier F., Rawlings S., 2009b, *ApJ*, **703**, 1890
- Oku Y., Nagamine K., 2024, *ApJ*, **975**, 183
- Oman K. A., 2022, *MNRAS*, **509**, 3268
- Papastergis E., Martin A. M., Giovanelli R., Haynes M. P., 2011, *ApJ*, **739**, 38
- Qin F., Howlett C., Staveley-Smith L., 2019, *MNRAS*, **487**, 5235
- Qin F., Howlett C., Parkinson D., 2025, *ApJ*, **978**, 7
- Sancisi R., Fraternali F., Oosterloo T., van der Hulst T., 2008, *A&ARv*, **15**, 189
- Schaye J., et al., 2015, *MNRAS*, **446**, 521
- Schaye J., et al., 2023, *MNRAS*, **526**, 4978
- Sofue Y., Rubin V., 2001, *ARA&A*, **39**, 137
- Somerville R. S., Popping G., Trager S. C., 2015, *MNRAS*, **453**, 4337
- Sorce J. G., Tully R. B., Courtois H. M., Jarrett T. H., Neill J. D., Shaya E. J., 2014, *MNRAS*, **444**, 527
- Spergel D. N., et al., 2003, *ApJS*, **148**, 175
- Spinelli M., Zoldan A., De Lucia G., Xie L., Viel M., 2020, *MNRAS*, **493**, 5434
- Springel V., et al., 2005, *Nature*, **435**, 629
- Springel V., et al., 2018, *MNRAS*, **475**, 676
- Springob C. M., Masters K. L., Haynes M. P., Giovanelli R., Marinoni C., 2007, *ApJS*, **172**, 599
- Stevens A. R. H., Sinha M., Rohl A., Sammons M. W., Hadzhiyska B., Hernández-Aguayo C., Hernquist L., 2024, *Publ. Astron. Soc. Australia*,

- 41, e053
- Taylor E. N., et al., 2023, *The Messenger*, 190, 46
- Trujillo-Gomez S., Klypin A., Primack J., Romanowsky A. J., 2011, *ApJ*, 742, 16
- Tully R. B., Fisher J. R., 1977, *A&A*, 54, 661
- Tully R. B., Fouque P., 1985, *ApJS*, 58, 67
- Tully R. B., et al., 2023, *ApJ*, 944, 94
- Tumlinson J., Peebles M. S., Werk J. K., 2017, *ARA&A*, 55, 389
- Vijayan A. P., Clay S. J., Thomas P. A., Yates R. M., Wilkins S. M., Henriques B. M., 2019, *MNRAS*, 489, 4072
- Watkins R., et al., 2023, *MNRAS*, 524, 1885
- Weltman A., et al., 2020, *Publ. Astron. Soc. Australia*, 37, e002
- Wilson T. L., Rohlfis K., Hüttemeister S., 2013, *Tools of Radio Astronomy*. Springer, doi:10.1007/978-3-642-39950-3
- Xie L., De Lucia G., Hirschmann M., Fontanot F., Zoldan A., 2017, *MNRAS*, 469, 968
- Xie L., De Lucia G., Hirschmann M., Fontanot F., 2020, *MNRAS*, 498, 4327
- Yahya S., Bull P., Santos M. G., Silva M., Maartens R., Okouma P., Bassett B., 2015, *MNRAS*, 450, 2251
- Yates R. M., Henriques B., Thomas P. A., Kauffmann G., Johansson J., White S. D. M., 2013, *MNRAS*, 435, 3500
- Yates R. M., Henriques B. M. B., Fu J., Kauffmann G., Thomas P. A., Guo Q., White S. D. M., Schady P., 2021a, *MNRAS*, 503, 4474
- Yates R. M., Péroux C., Nelson D., 2021b, *MNRAS*, 508, 3535
- Yates R. M., Hendriks D., Vijayan A. P., Izzard R. G., Thomas P. A., Das P., 2024, *MNRAS*, 527, 6292
- York D. G., et al., 2000, *AJ*, 120, 1579
- Yung L. Y. A., et al., 2022, *MNRAS*, 515, 5416
- Yung L. Y. A., et al., 2023, *MNRAS*, 519, 1578
- Zhang K., et al., 2019, *Science China Physics, Mechanics, and Astronomy*, 62, 959506
- Zhang C.-P., et al., 2024, *Science China Physics, Mechanics, and Astronomy*, 67, 219511
- Zoldan A., De Lucia G., Xie L., Fontanot F., Hirschmann M., 2017, *MNRAS*, 465, 2236
- Zoldan A., De Lucia G., Xie L., Fontanot F., Hirschmann M., 2018, *MNRAS*, 481, 1376
- Zoldan A., De Lucia G., Xie L., Fontanot F., Hirschmann M., 2019, *MNRAS*, 487, 5649
- Zwaan M. A., Meyer M. J., Staveley-Smith L., Webster R. L., 2005, *MNRAS*, 359, L30
- de Blok W. J. G., Walter F., Brinks E., Trachternach C., Oh S. H., Kennicutt Jr. R. C., 2008, *AJ*, 136, 2648

This paper has been typeset from a $\text{\TeX}/\text{\LaTeX}$ file prepared by the author.